Bioactive Materials 16 (2022) 95–106

Contents lists available at ScienceDirect

Bioactive Materials

journal homepage: www.keaipublishing.com/en/journals/bioactive-materials

Alloyed nanostructures integrated metal-phenolic nanoplatform for synergistic wound disinfection and revascularization

Yi Xie [a], Shengqiu Chen [a], Xu Peng [c], Xiaoling Wang [b], Zhiwei Wei [a], Joseph J. Richardson [e], Kang Liang [d], Hirotaka Ejima [e], Junling Guo [a,b,f,*], Changsheng Zhao [a,g,**]

[a] College of Polymer Science and Engineering, State Key Laboratory of Polymer Materials Engineering, Sichuan University, Chengdu, Sichuan, 610065, China
[b] BMI Center for Biomass Materials and Nanointerfaces, College of Biomass Science and Engineering, Sichuan Univerisity, Chengdu, Sichuan, 610065, China
[c] Laboratory Animal Center, Sichuan University, Chengdu, Sichuan, 610065, China
[d] School of Chemical Engineering, Graduate School of Biomedical Engineering, and Australian Centre for NanoMedicine, University of New South Wales, Sydney, NSW, 2052, Australia
[e] Department of Materials Engineering, School of Engineering, The University of Tokyo, 7−3−1 Hongo, Bunkyo-ku, Tokyo, 113−8656, Japan
[f] Bioproducts Institute, Departments of Chemical and Biological Engineering, The University of British Columbia, Vancouver, BC, V6T 1Z4, Canada
[g] School of Chemical Engineering, Sichuan University, Chengdu, Sichuan, 610065, China

ARTICLE INFO

Keywords:
Metal-phenolic network
Wound healing
Antibacterial activity
Revascularization

ABSTRACT

New materials for combating bacteria-caused infection and promoting the formation of microvascular networks during wound healing are of vital importance. Although antibiotics can be used to prevent infection, treatments that can disinfect and accelerate wound healing are scarce. Herein, we engineer a coating that is both highly compatible with current wound dressing substrates and capable of simultaneously disinfecting and revascularizing wounds using a metal-phenolic nanoplatform containing an alloyed nanostructured architecture (Ag@Cu-MPN_{NC}). The alloyed nanostructure is formed by the spontaneous co-reduction and catalytic disproportionation reaction of multiple metal ions on a foundation metal-phenolic supramolecular layer. This synergistic presence of metals greatly improves the antibacterial activity against both Gram-negative and Gram-positive pathogenic bacteria, while demonstrating negligible cytotoxicity to normal tissue. In infected rat models, the Ag@Cu-MPN_{NC} could kill bacteria efficiently, promoting revascularization and accelerate wound closure with no adverse side effects in infected in *vivo* models. In other words, this material acts as a combination therapy by inhibiting bacterial invasion and modulating bio-nano interactions in the wound.

1. Introduction

Impaired wound healing and its medical complications result in a large morbidity and mortality burden worldwide [1–6]. Various factors influence wound healing, and therefore materials capable of promoting regeneration in real-world setting need to interact with different biological agents simultaneously [7–11]. For example, the regeneration of injured tissue during wound healing requires the proliferation and migration of fibroblasts and keratinocytes [12,13], which collectively re-establish the normal cellular and extracellular matrix composition of the skin and facilitate the growth of vascular endothelial cells (i.e., new blood vessels) [14–16]. However, the presence of bacteria can impair the differentiation of fibroblasts, thereby inhibiting normal wound healing while simultaneously compromising the immune system [17]. Bacterial infection is one of the most frequent and severe complications for wound healing [18,19], and the treatment with antibiotics is the gold-standard protocol used in the clinic [20]. However, antibiotics by themselves do not promote would healing, and the excessive use of antibiotics leads to drug resistant bacteria and can also cause various side effects [21–24]. Moreover, there is a dearth of new antibiotics in the clinical pipeline. Therefore, substantial efforts have been dedicated to developing new antimicrobial materials in the lab, including nanozymes

Peer review under responsibility of KeAi Communications Co., Ltd.
* Corresponding author. BMI Center for Biomass Materials and Nanointerfaces, School of Biomass Science and Engineering, Sichuan University, Chengdu, Sichuan, 610065, China.
** Corresponding author. College of Polymer Science and Engineering, State Key Laboratory of Polymer Materials Engineering, Sichuan University, Chengdu, Sichuan, 610065, China.
E-mail addresses: junling.guo@scu.edu.cn, junlingguo@g.harvard.edu, junling.guo@ubc.ca (J. Guo), zhaochsh70@163.com, zhaochsh70@scu.edu.cn (C. Zhao).

https://doi.org/10.1016/j.bioactmat.2022.03.004
Received 21 December 2021; Received in revised form 22 February 2022; Accepted 3 March 2022
Available online 19 March 2022

[1,25–27], metal or metal oxide nanoparticles [28–36], metal-organic networks [3,37], cationic polymers [38–40], dendrimeric peptides [41–44], carbon-based nanostructures [45], nanocellulose-based materials [46], and supramolecular complexes [47–50].

Antimicrobial metals, instead of antibiotic small molecules, were historically used to treat infection and have recently re-emerged as a promising strategy to inhibit the growth of bacteria and promote wound healing [51–53]. Among the most promising metals, silver nanoparticles (AgNPs) have been intensively studied and shown high efficiency and broad-spectrum antimicrobial activity [54–56]. Nevertheless, growing evidence shows that AgNPs can also cause undesirable cytotoxic and genotoxic effects, and bimetallic antimicrobial systems (e.g., Fe–Ag, Pt–Pd, Co–Au, etc.) have recently been developed with significantly enhanced antibacterial efficacy and lower side effects due to the synergism of the two metallic components [57–65]. However, the synthesis of bimetallic alloys capable of being integrated with conventional wound dressings is generally complicated and often involves the use of organic solvents or potentially toxic substrates, and the in vivo biosafety profiles of these materials are generally neglected in the previous studies [66]. An ideal platform for enhancing wound healing in clinical settings would therefore allow for any wound dressing material to be readily endowed with antimicrobial and tissue revascularization properties, simultaneously [67,68].

Metal-phenolic networks (MPNs) are a versatile class of biocompatible materials constructed from natural polyphenols and metal ions through coordination bonds [69]. In our previous studies, we demonstrated that the functionality of MPNs can be tuned by varying the incorporated metal ions (Fe^{3+}, Al^{3+}, Sm^{3+}, etc.) [70], which has allowed for the rational design of diverse MPN-based materials for biomedical and energy applications [71–74]. Importantly, the ability of MPNs to incorporate multiple metals into a single coating inspires that they could be used to combine antibacterial and tissue regeneration properties, and currently no previous studies have shown the ability of MPNs to integrate alloyed nanostructures in situ during the surface functionalization process. Herein, we engineer various medical substrates with the synergistic effects of disinfection and revascularization using a bimetallic

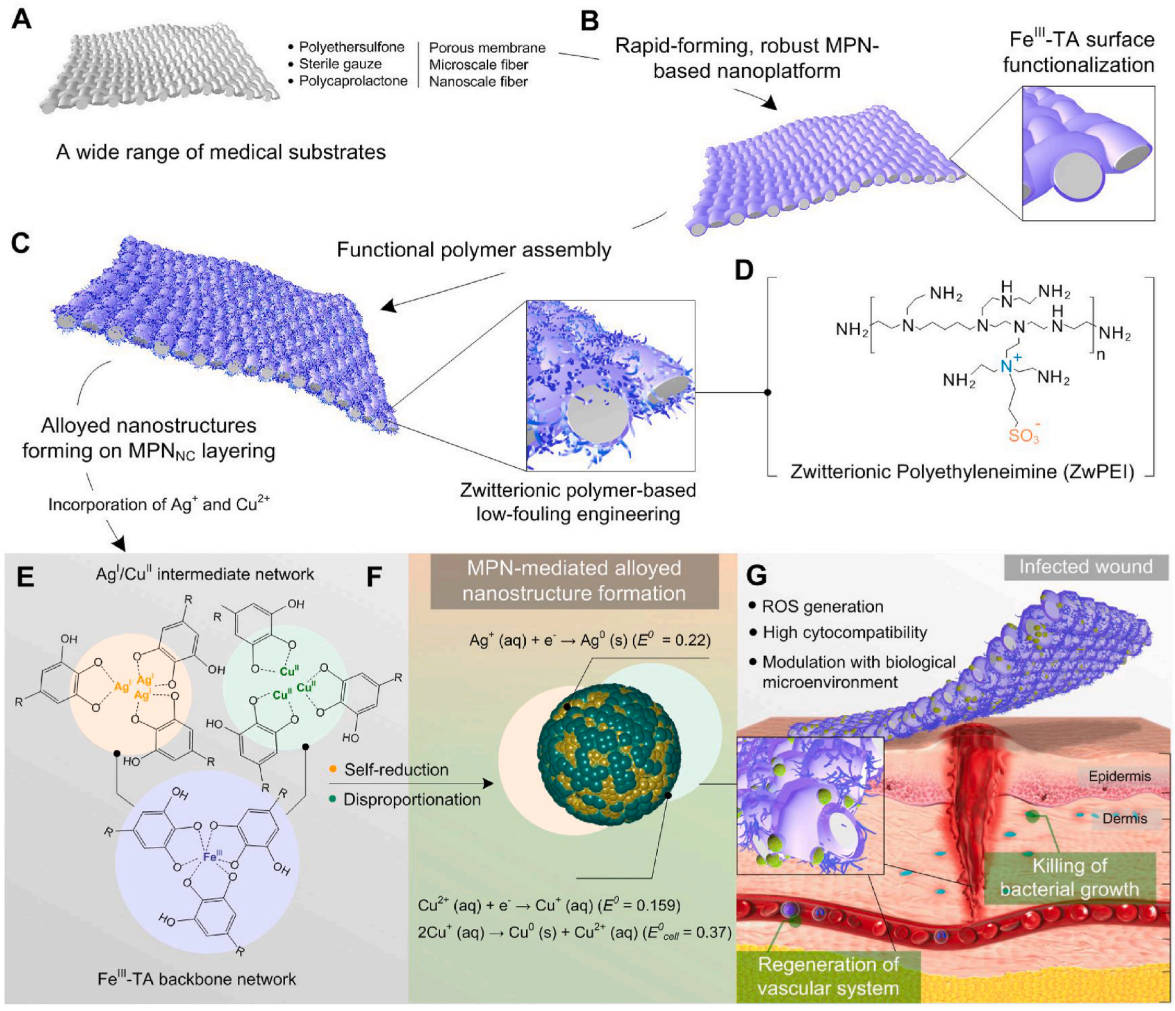

Fig. 1. Metal-phenolic nanoplatform with bimetallic alloyed nanostructures and their synergistic effects on disinfection and vascular regeneration. (A) Surface-adaptive functionalization property of the MPN-based coating on various clinical wound healing substrates. (B) The surface functionalization of Fe^{III}-TA enables a rapid and robust platform for the engineering of multifunctional coating surfaces. (C) Zwitterionic polymers can be assembled on the Fe^{III}-TA surface, imparting low-fouling to the surface. (D) Molecular structure of zwitterionic PEI. The colors indicate the separate positively and negatively charged groups. (E) Schematic illustration of the multiple domains of the MPN-based system. The Fe^{III}-TA network anchors the foundation layer of the coating on medical substrates due to its versatile coating capability. The free catechol/galloyl groups of the Fe^{III}-TA network can further chelate Ag^+ and Cu^{2+} ions. (F) The redox potential of the phenolic groups enables the self-reduction of Ag^+ to metallic Ag, while the Cu^{2+} can be reduced to Cu^+, followed by a disproportionation reaction. These reactions lead to the formation of MPN-supported Ag@Cu alloyed nanostructures on the Fe^{III}-TA network coating. (G) Schematic illustration of the therapeutic effects of the multifunctional MPN-based coating on medical substrates, which involve the ROS-mediated killing of bacteria and the stimulation of revascularization. The bimetallic alloyed nanostructure (magnified boxes) provides a high cytocompatibility compared with traditional bimetallic antibacterial materials.

and nanostructured MPN coating (Fig. 1). An initial iron (III)-tannic acid (Fe^{III}-TA) layer capped with zwitterionic low-fouling polymer (ZwPEI) is used to engineer bimetallic nanoparticles, thereby leading to a MPN coating integrated with alloyed nanostructures (referred as Ag@Cu-MPN_{NC}). The Ag@Cu-MPN_{NC}-modified surfaces demonstrated efficient antimicrobial activity to both Gram-positive and Gram-negative bacteria, without any off-target effects on mammalian cells. Importantly, the Ag@Cu-MPN_{NC} showed a remarkable therapeutic effect on accelerating wound healing in animals with infected skin wounds by reducing inflammation and promoting revascularization of the injured tissue.

2. Experiment section

2.1. Preparation of metal-phenolic nanoplatform of Ag@Cu-MPN_{NC}

PES ultrafiltration membranes (PES), commercial PES microfiltration (MF) membranes, polycaprolactone (PCL) electrospinning nanofiber membranes (NFM), and gauze were chosen as substrates for conducting the preparation of surface-adaptive Ag@Cu-MPN_{NC}. The standard coating process can be described as: PES membranes were first incubated with an aqueous TA solution (1 mg mL^{-1}) for 5 min under gentle shaking. Then, the membranes were transferred into aqueous $FeCl_3$ solution (0.5 mg mL^{-1}) for 5 min. After that, obtained Fe^{III}-TA-functionalized PES were washed for 2–3 times with DI water. Then, Fe^{III}-TA-functionalized PES were incubated with pre-prepared zwitterionic polymer (ZwPEI) solution (1 mg mL^{-1}) and TA solution (1 mg mL^{-1}) for 10 min respectively with five times repeats to obtain the MPN_{NC}-PES. After that, the MPN_{NC}-PES were incubated with $AgNO_3$ solution, $Cu(NO_3)_2$ solution, or $AgNO_3$/$Cu(NO_3)_2$ mixture solutions with 0.1 mol mL^{-1} Ag^+ and Cu^{2+} to construct metal-phenolic nanoplatforms which were termed as Ag-MPN_{NC}-PES, Cu-MPN_{NC}-PES, and Ag@Cu-MPN_{NC}-PES, respectively.

2.2. Antibacterial activity evaluation

The antibacterial activity of the Ag@Cu-MPN_{NC}-PES was measured by optical density (OD) monitoring and blood agar (SBA) plate counting. After 10^6 CFU mL^{-1} bacterial liquid was co-cultured with the membrane, the membrane was removed out and the optical density at 600 nm (OD_{600}) for bacterial liquid was measured by UV–vis spectra to study the bacterial inhibition efficiency of the membranes. For SBA plate counting, the co-cultured solution was diluted in series with saline at a proper scale and then 100 μL bacterial suspension added on an SBA plate for counting the number of living bacterial cells. The bactericidal ratio can be quantified by counting the number of colonies on the plates recorded by the digital camera according to the following equation:

$$\text{Antibacterial efficiency } (\%) = (CFU_{control} - CFU_{sample})/(CFU_{control}) \times 100\%$$

As for bacterial attachment on the membranes, the LIVE/DEAD bacteria staining was applied after 12 h of incubation using Bac-Light viability kit (SYTO-9 for live bacteria and propidium iodide (PI) for dead bacteria) and then the adhered bacteria were observed by fluorescence microscopy (DMI8, Leica). Meanwhile, the adhered bacteria were visualized using SEM after being fixed by fresh prepared glutaraldehyde (2.5 wt %) and dehydrated by ethanol solutions with a series of concentrations.

2.3. Cytotoxicity assay

Cytotoxicity test of the membranes were carried with CCK-8 assay with L929 cells. L929 cells were grown in complete medium containing DMEM. 100 μL of the cells was seeded on a 24-well tissue culture polystyrene plate (control) or membranes at a density of 0.7×10^4 cells/cm^2. After 1 h, another 400 μL of the culture medium was added. A series of incubation time scale was set up for this cytotoxicity test: 1, 3, 5 and 7 days. At each time point, 50 μL of CCK-8 assay solution was added to each well and incubated at 37 °C for 1 h, and then the optical density (OD) of each well was determined with a Microplate reader (Multiskan Sky, Thermo Fisher, USA) at 450 nm.

2.4. Hemolysis assay

5 mL of whole blood was added to 10 mL of calcium- and magnesium-free PBS solution, and then red blood cells (RBCs) were isolated from plasma by 5 times centrifuging. The obtained RBCs were diluted in PBS to a volume of 100 mL for further use. For the hemolysis test, 0.2 mL of the diluted RBCs suspension (around 5×10^8 cells/mL) was added to 0.8 mL of normal saline which containing one piece of membrane. The RBCs solution dispersed in normal saline was selected as a negative control and RBCs solution dispersed in DI water was used as a positive control. All the suspensions were centrifuged at 1000 rpm for 3 min after being incubated in a rocking shaker at 37 °C for 3 h. The absorbance of the released hemoglobin was measured at 540 nm by a UV–vis spectrometer (UV-1750, Shimadzu Co., Ltd, Japan), and then the hemolysis ratio was calculated according to the following equation:

$$\text{Hemolysis ratio } (\%) = (A_s\text{-}A_n) / (A_p\text{-}A_n) \times 100\%$$

where A_s is the absorbance of the suspensions in the presence of the sample, A_p and A_n are the absorbance of positive and negative controls, respectively.

2.5. Mechanistic study of reactive oxygen species (ROS) generation

The antibacterial efficacy of Ag@Cu-MPN_{NC}-PES might be associated with the generation of ROS, which could be detected by the electron paramagnetic resonance (EPR, Bruker EMX Plus, Billerica, Massachusetts, USA). Briefly, a piece (1×1 cm^2) of membrane was immersed in 1 mL normal saline and 50 μL 5,5-dimethyl-1-pyrroline-N-oxide (DMPO) was added to the solution for 5 min to trap •OH in the form of the spin adduct DMPO/•OH. Then, the EPR spectrum was recorded. Meanwhile, $^1O_2$ was also detected and 2,2,6,6-tetramethylpiperidine (TEMP) was used to trap $^1O_2$. 50 mM TEMP was added to the solution and the EPR spectrum was recorded. To detect the level of bacterial intracellular ROS, 2′,7′-dichlorofluorescin diacetate (DCFH-DA) was employed. *S. aureus* cells were respectively inoculated with a piece (1×1 cm^2) of membranes at 37 °C for 4 h. Then, the bacterial incubating with 10 μM DCFH-DA at 37 °C for 30 min. After that, the fluorescence intensity was detected at excitation/emission wavelength of 488/525 nm.

2.6. Experimental rat wound mode

Sprague dawley (SD) mice (220–250 g, male, 6–8 weeks) were purchased from Chengdu Dossy Biological Technology Co. Ltd. (China) and used for in vivo studies. All animal experimental procedures were approved by Sichuan University Animal Ethics Committee in concordance with the Principles of Laboratory Animal Care formulated by the National Society for Medical Research. The SD mice were firstly anesthetized using 2% sodium pentobarbital. After shaving and disinfecting with iodophor, 8 mm round skin injuries were made on the back of mice and then 100 μL of *S. aureus* dispersion (10^8 CFU/mL) was injected onto the wound.

After injection of bacteria and cultured for 24 h, the PCL-based NFMs and metal-phenolic nanoplatform decorated NFMs were directly employed to treat the wound as wound dressing. Mice with established infection wounds were then randomly assigned to the following groups (three mice per group): (1) untreated control, (2) NFM treated, (3) MPN_{NC}-NFM, (4) Ag-MPN_{NC}-NFM and (5) Ag@Cu-MPN_{NC}-NFM.

After 2, 6, 10, and 14 days of supervision, the wound area was imaged by a digital camera and the wound healing ratio was measured

based on the following equation:

$$\text{Wound healing ratio (\%)} = [W_0 - \text{Wound}_{(2,6,10,14\ \text{days})} / W_0] \times 100\%$$

where $\text{Wound}_{(2,6,10,14\ \text{days})}$ represents the wound area (mm^2) after 2, 6, 10, and 14 days, respectively, and W_0 represents the initial wound area. After 14 days, these treated wound skin tissues and internal organs were gathered for immunohistochemical and immunofluorescence staining, and histological analysis.

2.7. Experimental pig skin disinfection mode

In vitro sterile pig skin was used as a model skin, and then the skin disinfection test was performed. The pig skins were first cut into small pieces (3 cm × 3 cm). Subsequently, for each skin, a groove-shape rectangle portion was removed by skin graft blade to afford wounds with a consistent size of 1 cm × 0.5 cm. Each wound was inoculated with 100 μL of bacterial dispersion in Mueller-Hinton Broth (MHB, the concentration was fixed to ~10^8 CFU mL^{-1}) and then treated with different membranes after incubation at 37 °C for 30 min. After 16 h, each wound was rinsed with saline for 3 times, and the pictures of wound were captured by digital camera. The adhered *S. aureus* on pig skins were visualized using SEM (JSM-7500F, Japan) after being fixed by fresh prepared glutaraldehyde (2.5 *wt* %) and dehydrated by ethanol solutions with a series of concentrations.

3. Results and discussion

3.1. Design strategy and structural characterization of Ag@Cu-MPN$_{NC}$

The synthesis of Ag@Cu-MPN_{NC} nanoplatform on different substrates was inspired by classic MPN chemistry (Fig. 1) [70,75]. A polyethersulfone (PES) membrane, a typical biomaterial used in blood purification, was first employed as a substrate for the demonstration of Ag@Cu-MPN_{NC} synthesis. The PES was first functionalized with a Fe^{III}-TA coating layer yielding MPN_{NC} (Fig. 1A,B, Fig. S1), followed by the adsorption of zwitterionic polymer ZwPEI to construct an antifouling surface (Fig. 1C and D) [76,77]. Fourier-transform infrared spectroscopy (FTIR) spectra showed the corresponding characteristic peaks at 1205 cm^{-1} (C–O vibration of TA), 1740 cm^{-1} (C═O vibration of TA), and 1030 cm^{-1} ($S(=O)_2$–OH vibration of ZwPEI) (Fig. S2) [59]. High-resolution N_{1s} spectrum showed two characteristic peaks located at 398.1 eV and 401.2 eV, which further agrees with the functionalization of zwitterionic polymers on the Fe^{III}-TA surface (Fig. 2A, C). Meanwhile, the elemental compositions of the membrane surfaces determined by XPS analysis are also indicates the contents of zwitterionic polymers on the Fe^{III}-TA surface.

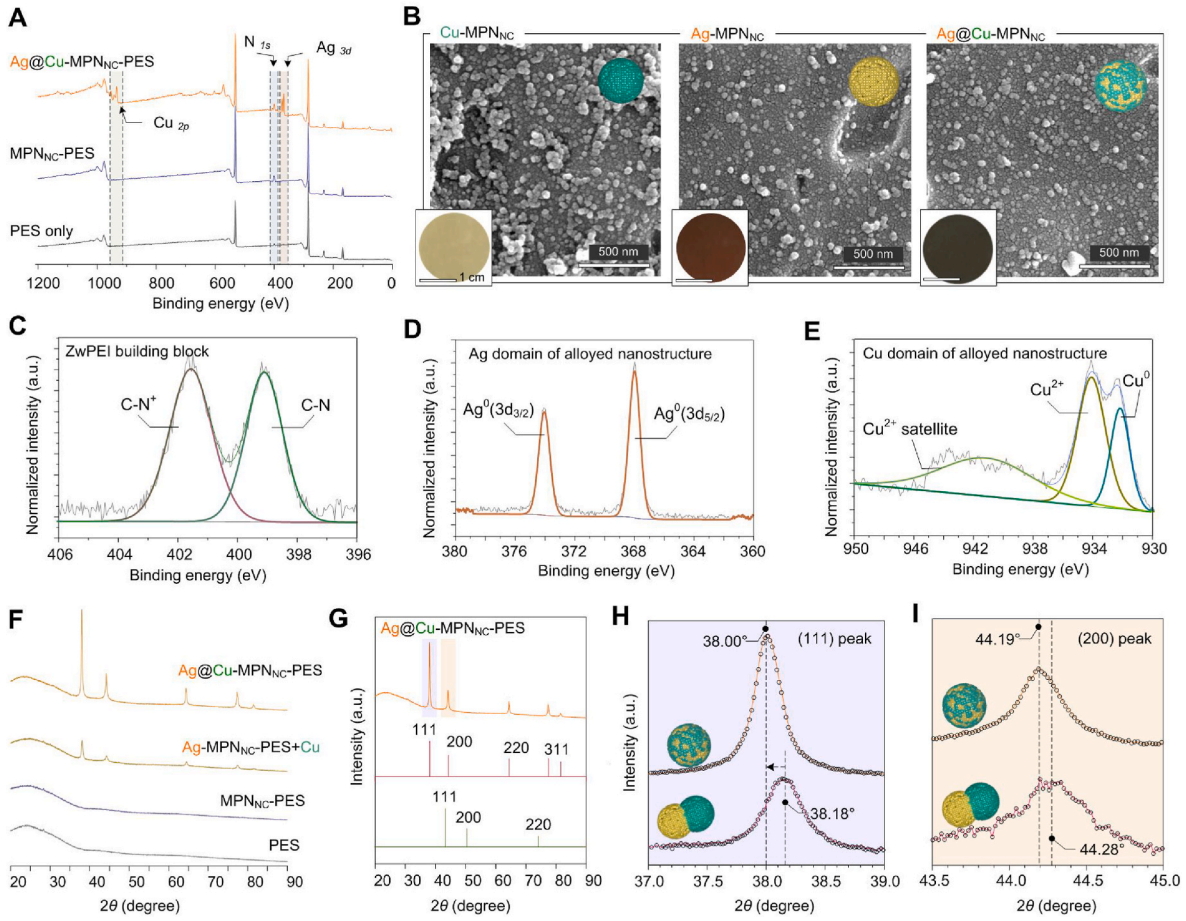

Fig. 2. Characterization of the metal-phenolic-functionalized surface integrated with the bimetallic alloyed nanostructures. (A) SEM images of MPN_{NC} integrated with different species of metallic systems. The insets are photographs of the coatings on the PES, where distinct colors are corresponded to the incorporated metals. (B) XPS survey scan spectra for native PES, MPN_{NC}, and Ag@Cu-MPN_{NC}-PES. In the Ag@Cu-MPN_{NC}-PES spectrum, the peaks of Ag_{3d} and Cu_{2p} indicate the formation of bimetallic nanostructures. The peak of N_{1s} supports the assembly of ZwPEI polymers on Fe^{III}-TA foundation layer. (C–E) High-resolution XPS spectra of N_{1s}, Ag_{3d}, and Cu_{2p}, showing the element states of each functional domain. (F) XRD patterns of Ag@Cu-MPN_{NC}-PES and the corresponding controls. Ag@Cu-MPN_{NC}-PES and Ag-MPN_{NC}-PES samples show distinct crystalline peaks, and in contrast, MPN_{NC} only presents amorphous structure (only Fe^{III}-TA foundation layer). (G) Comparison of Ag@Cu-MPN_{NC}-PES with the standard peaks of metallic silver and copper. (H–I) XRD spectra of Ag (111) and (200) peaks of Ag@Cu-MPN_{NC}-PES and Ag -MPN_{NC}-PES with the post-addition of Cu^{2+} ions. The shifts of the XRD peaks were ascribed to the formation of alloyed Ag@Cu nanostructures.

To synthesize the alloyed nanostructures, Ag^{+} and Cu^{2+} ions were added and incorporated onto PES membrane via the coordination interaction between the catechol/galloyl groups of the MPN_{NC} layer to form Ag^{I}/Cu^{II}-TA (Fig. 1E). During this alloying process, Ag^{+} ions can be self-reduced to AgNPs due to the reduction ability of catechol or galloyl groups [78], and scanning electron microscopy (SEM) images showed a slight increase in particle size between the bimetallic Ag@Cu-MPN_{NC} system (34.1 ± 6.2 nm) compared to the monometallic Ag-MPN_{NC} system (32.0 ± 4.8 nm) (Fig. 2B, Fig. S3). Interestingly, the incorporated Cu^{2+} ions can be also co-reduced to Cu^{+}, spontaneously progressing a disproportionation reaction of $2Cu^{+}$ (aq) → Cu^{0} (s) + Cu^{2+} (aq) (E^{0}_{cell} = 0.37) (Fig. 1F). High-resolution XPS spectra of Cu_{2p} indicated the presence of Cu^{0} and Cu^{2+} at 933.2 and 935.0 eV, respectively (Fig. 2E) [79–81]. Meanwhile, energy dispersive X-ray spectroscopy (EDS) mapping images further confirmed the presence and high distribution of Cu and Ag in the microstructure of Ag@Cu-MPN_{NC} while still retaining the N signal from ZwPEI (Fig. 2A, Fig. S4). X-ray powder diffraction (XRD) patterns of the Ag@Cu-MPN_{NC} exhibited several peaks located at 2θ = 38.0, 44.2, 64.4, 77.3, and 81.4° (Fig. 2F). Notably, when compared against the typical Ag patterns [ICDD 04–0783] for the (111) plane of monometallic Ag (2θ = 38.2°) and Ag-MPN_{NC} with the post-addition of Cu^{2+} ions (2θ = 38.18°), the Ag (111) peak of Ag@Cu-MPN_{NC} shifted slightly to a lower angle at 2θ = 38.0° (Fig. 2G and H). Similar shifts could also be observed on the Ag (200) peak of Ag@Cu-MPN_{NC} (2θ = 44.19°) in comparison to monometallic Ag-MPN_{NC} with the post-addition of Cu^{2+} ions (2θ = 44.28°) (Fig. 2I). These results support the formation of Ag–Cu alloys on the MPN_{NC} foundation layer via the catechol/galloyl-facilitated co-reduction process.

The anti-fouling surface/interface is very important for biomaterials to resist protein adsorption as candidates for preventing bacterial adhesion. The hydrophilicity of the bio-materials surface would induce a strong hydration layer formation at the interface, which plays a key role for antifouling performance to resist the nonspecific protein adsorption and bacterial adhesion. In addition, the water contact angles (WCAs) for pristine PES and Ag@Cu-MPN_{NC}-functionalized membranes (Ag@Cu-MPN_{NC}-PES) were measured, as the hydrophilicity of bandages is a potential indicator for biocompatibility and beneficial to wound healing (Fig. S5) [25,82]. The bare PES had a WCA of ~80°, while the MPN_{NC} had a WCA of ~39°, indicating a significant improvement of surface hydrophilicity, which was ascribed to both the hydrophilic phenolic building blocks and hydrophilic ZwPEI. After the integration of the bimetallic nanostructures, the Ag@Cu-MPN_{NC}-functionalized surface exhibited significantly lowered WCA values (~30°) due to the introduction of the hydrophilic Ag–Cu alloyed NPs. Overall, the integration of these three building blocks (natural polyphenols, zwitterionic polymers, and metal nanoparticles) improve the hydrophilicity of the

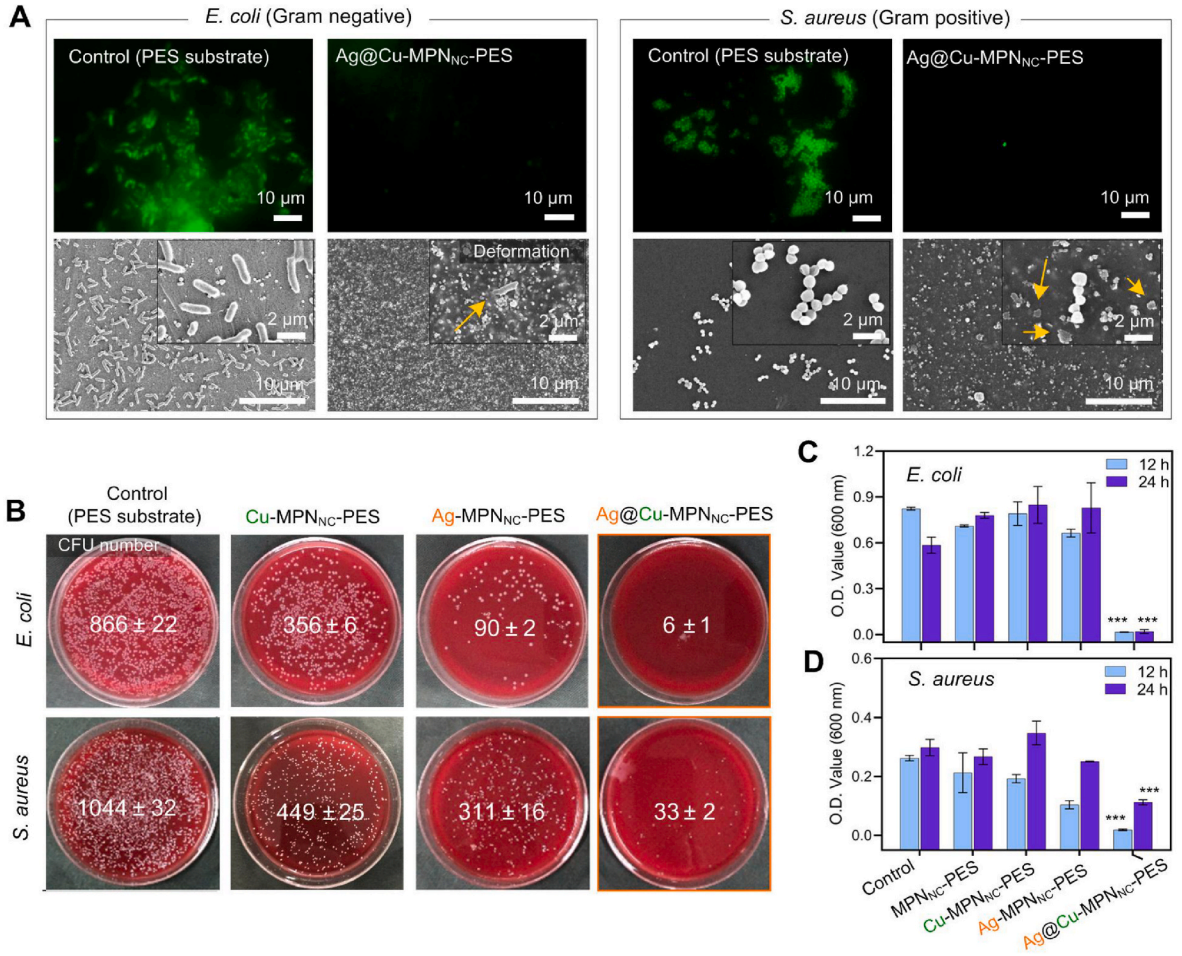

Fig. 3. Antibacterial properties against both Gram-negative and Gram-positive pathogenic strains. (A) Representative fluorescence and SEM microscopy images for pristine PES and the Ag@Cu-MPN_{NC} after being cultured with *E. coli* and *S. aureus* for 12h. Bacteria were stained with SYTO 9 green fluorescent nucleic acid stain for the observation under fluorescence microscopy. Orange arrows indicate the deformed and destroyed bacteria. (B) Representative photographs of bacterial colonies formed on sheep blood agar (SBA) plates treated with different membranes. The values show the numbers of counted colonies (X 10^{4} CFU). (C–D) OD_{600} values of *E. coli* and *S. aureus* samples after 12h- and 24h-incubation with different membranes. Variation is represented by SE (error bars) from three independent replicates for all data points, *** (p-value < 0.05). The cell density of the group treated with Ag@Cu-MPN_{NC}-PES showed a significant difference compared with the other groups.

surface, which is beneficial to the crucial bio-material interactions for wound healing [25].

3.2. Antibacterial performance and mechanistic study of Ag@Cu-MPN$_{NC}$

To estimate the antibacterial performance of Ag@Cu-MPN$_{NC}$, *Escherichia coli* (Gram negative, *E. coli*: ATCC, 25922) and *Staphylococcus aureus* (Gram positive, *S. aureus*: ATCC, 6538) were chosen as model pathogenic bacteria and incubated with the membranes for 12 h before imaging the bacteria proliferation. Pristine PES showed no antibacterial property to these pathogenic strains, as a significant amount of aggressively growing bacteria could be seen (Fig. 3A, Fig. S6, Fig. S7). However, the amounts of both *E. coli* and *S. aureus* on the Ag@Cu-MPN$_{NC}$-functionalized membrane (Ag@Cu-MPN$_{NC}$-PES) surfaces were significantly decreased. Moreover, an obvious deformation of the microbes was observed due to the combined effects of the anti-fouling ZwPEI layers and the antibacterial alloyed nanostructures. To quantitatively evaluate the antibacterial capabilities, bacterial suspensions were co-cultured with different membranes and the numbers of colony-forming units (CFUs) were determined (Fig. 3B). The membranes functionalized with monometallic Cu (Cu-MPN$_{NC}$-PES) had moderate antibacterial activity (58.9% for *E. coli* and 56.9% for *S. aureus*, Fig. S8), while the monometallic Ag-MPN$_{NC}$-PES exhibited a slightly increased antibacterial activity (89.6% for *E. coli* and 70.2% for *S. aureus*). Notably, only few bacteria were observed on the surface of Ag@Cu-MPN$_{NC}$-PES, and the antibacterial ratios were ~100% against both strains. The optical density at 600 nm (OD_{600}) showed similar antibacterial performance on each sample (Fig. 3C and D). These results demonstrated that the alloyed nanoarchitectures engineered on the MPN$_{NC}$ surface endowed the membranes with enhanced killing efficiency in comparison to the monometallic systems.

The superior antibacterial properties of the Ag@Cu-MPN$_{NC}$ against both Gram-positive and Gram-negative pathogenic strains motivated us to understand the mechanism for the enhanced antibacterial activity. Electron paramagnetic resonance (EPR) measurement was applied to probe the generation of reactive oxygen species (ROS) [83]. 5,5-dimethyl-1-pyrroline-N-oxide (DMPO) was selected as spin traps for hydroxyl radical (·OH) detection. After the incubation with monometallic Ag-MPN$_{NC}$, a weak EPR signal was observed, while an intense EPR signal was exhibited after 10 min incubation with bimetallic Ag@Cu-MPN$_{NC}$ membrane (Fig. 4A). Interestingly, a similar level of strong EPR signals was also observed after the incubation with Cu-MPN$_{NC}$, suggesting that the generation of ROS can be mainly ascribed to the Cu domain of the alloyed system. Meanwhile, the representative DMPO-OH adduct was not observed in the Cu-MPN$_{NC}$, which could result from the interaction of Cu with DMPO and the formation of DMPO-dimers and carbon-centered radical adducts.

To further verify the species of the radicals, Dimethyl sulfoxide (DMSO) was added (a specific scavenger for ·OH) to investigate whether ·OH was involved in the EPR signal. After the addition of 40 wt% DMSO, the intensity of the EPR signal dramatically decreased, indicating the generation of ·OH in the reaction process (Fig. 4B). In addition, 2,2,6,6-tetramethylpiperidine (TEMP) was also selected as a spin trap for ROS detection. The EPR signals displayed a 1:1:1 triplet spectrum characteristic, demonstrating the generation of singlet oxygen ($^1O_2$) when encountering the Ag@Cu-MPN$_{NC}$ surface (Fig. 4C). A similar EPR signal was detected in the presence of free Cu^{2+} ions which further supported the generation of ROS due to the engineered Cu domain (Fig. S9). In addition, when NaN_3 (a specific scavenger for $^1O_2$) was added, the intensity of the EPR signal decreased dramatically. These results further confirmed that the active species generated by the Ag@Cu-MPN$_{NC}$ can be ascribed to $^1O_2$. These studies of ROS generation demonstrate that the Ag@Cu-MPN$_{NC}$ could accelerate the generation of two types of ROS (·OH and $^1O_2$) to kill pathogenic bacteria [84].

Although the monometallic Cu-MPN$_{NC}$ generated a similar level of ROS compared with Ag@Cu-MPN$_{NC}$, the coating engineered with the bimetallic alloyed nanostructures showed significantly higher antibacterial abilities. We rationalized that the intracellular oxidative stress in bacteria was different when encountering these two types of coatings [85]. Thus, 2′,7′-dichlorofluorescin diacetate (DCFH-DA) was used as a molecular probe to detect the level of intracellular oxidative stress. DCFH can penetrate into the cytosol of bacterial cells and be oxidized to DCF in the presence of ROS. Ag@Cu-MPN$_{NC}$ caused more than twice as much intracellular oxidative stress compared with those of monometallic Cu-MPN$_{NC}$ and Ag-MPN$_{NC}$ (Fig. 4D). These results revealed that the possible mechanism of the enhanced antibacterial ability of the Ag@Cu-MPN$_{NC}$ involves the generation of ROS ascribed to the Cu domain of the alloyed nanostructure. Synergistically, Ag is known to cause the disruption of cell membranes [86], leading to an efficient penetration of the generated ROS into the cytosol, which is known to oxidize intracellular proteins and disturb bacterial homeostasis. It is further demonstrated that the excellent antibacterial activity is not only

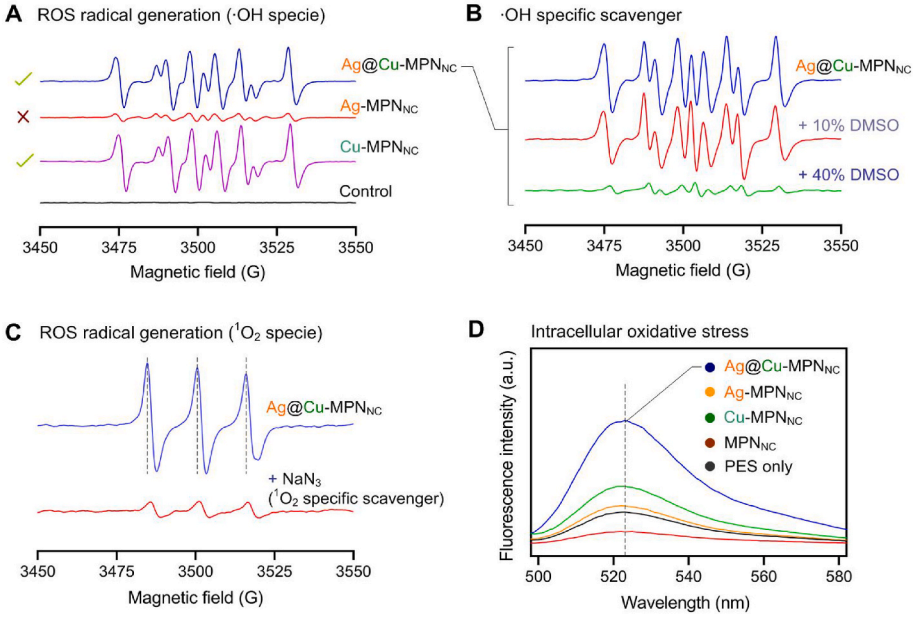

Fig. 4. Mechanistic study of the antibacterial properties for the bimetallic alloyed Ag@Cu-MPN$_{NC}$ coatings. (A) EPR spectra of DMPO/·OH adducts collected after 10 min-incubation of a 1 × 1 cm^2 membrane and 50 μL DMPO; (B) EPR spectra of DMPO/·OH adducts with different amounts of DMSO; (C) EPR spectra of $^1O_2$ after 20 min-incubation with Ag@Cu-MPN$_{NC}$-PES in the presence of TEMP; (D) Fluorescence spectra of bacteria treated with different membranes. The cells were stained with 2′,7′-dichlorodihydrofluorescein diacetate to indicate the generation of intracellular ROS levels.

original from the generated ROS, and the synergistic presence of metals plays a vital role for the antibacterial activity.

3.3. Biocompatibility and surface adaptability of Ag@Cu-MPN$_{NC}$

After demonstrating their robust antibacterial activity, the cytocompatibility of the Ag@Cu-MPN$_{NC}$ was investigated with a representative wound healing cell line, namely mouse fibroblasts L929. Fluorescence microscopy images showed that the antifouling ability of the Ag@Cu-MPN$_{NC}$-PES reduced the adhesion of L929 cells to the membrane when compared with bare PES (Fig. 5A). Though the initial attached cell number on the Ag@Cu-MPN$_{NC}$-PES was smaller than that of bare PES, the proliferation of L929 cells on the Ag@Cu-MPN$_{NC}$-PES showed a similar level with bare PES (Fig. 5B). The cell numbers increased continuously with the incubation time for bare PES, Cu-MPN$_{NC}$, and Ag@Cu-MPN$_{NC}$. The proliferation was significantly inhibited in the monometallic Ag-MPN$_{NC}$ sample, which was ascribed to the cytotoxicity of AgNPs. Interestingly, the proliferation of L929 was not affected by the alloyed Ag–Cu nanostructures on the membrane surface, though the content of Ag in Ag@Cu-MPN$_{NC}$ was almost the same as Ag-MPN$_{NC}$ (Table S1).

Meanwhile, hemolysis tests were performed to investigate the blood compatibility. The bare PES and MPN$_{NC}$-functionalized PES with no metallic nanostructures showed a low hemolysis ratio of ~1%. The presence of AgNPs in the Ag-MPN$_{NC}$-PES dramatically increased the hemolysis ratio to ~50% (Fig. 5C, Fig. S10). The Ag NPs can bind to thiol groups within biological moieties such as proteins or phospholipids of membrane with high affinity and thereby promote their denaturation [87], leading to osmotic lysis, membrane rupture or hemolysis [88]. No obvious hemolysis was observed in the sample incubated with Cu-MPN$_{NC}$, and notably the hemolysis ratio of Ag@Cu-MPN$_{NC}$-PES was as low as bare PES. These cell cytotoxicity and hemolysis tests demonstrated that the Ag@Cu-MPN$_{NC}$ have great promise for utilization in vivo [38]. Substrate-independent coatings are important, since medical components that interface with wounds, such as wound dressings and artificial implants, generally have different sizes, shapes, and material compositions depending on the specific therapeutic purposes [82]. Traditionally, each of these medical materials required a unique surface functionalization strategy, which in turn often required complicated procedures and the use of potentially cytotoxic compounds. Here, we applied this rapid and facile MPN-based alloyed nanostructured coating to three major substrates used in clinical applications, including PES microfiltration membrane (PES-MF), sterile gauze, and polycaprolactone nanofiber membrane (PCL-NFM). These three substrates have different microstructures and surface chemistries, and were functionalized with Ag@Cu-MPN$_{NC}$ to evaluate the antibacterial ability.

All the substrates changed color due to the MPN$_{NC}$ functionalization and the formation of the alloyed nanostructures (Fig. 5D–F). SEM images showed the variety of the microstructures of the three materials, which could be maintained after Ag@Cu-MPN$_{NC}$ functionalization. Moreover, the formation of highly dispersed nanostructures was observed in the SEM images. These materials were cultured with *E. coli* for 12 h, and it was found that the bacterial suspensions incubated with the Ag@Cu-MPN$_{NC}$-functionalized substrates remained clear with very few bacterial colonies. In contrast, the bare medical substrates had a high degree of bacteria growth with a turbid suspension after 12 h. These results demonstrate that our MPN-based strategy provides a simple and robust mean to impart a wide range of medical substrates with highly efficient

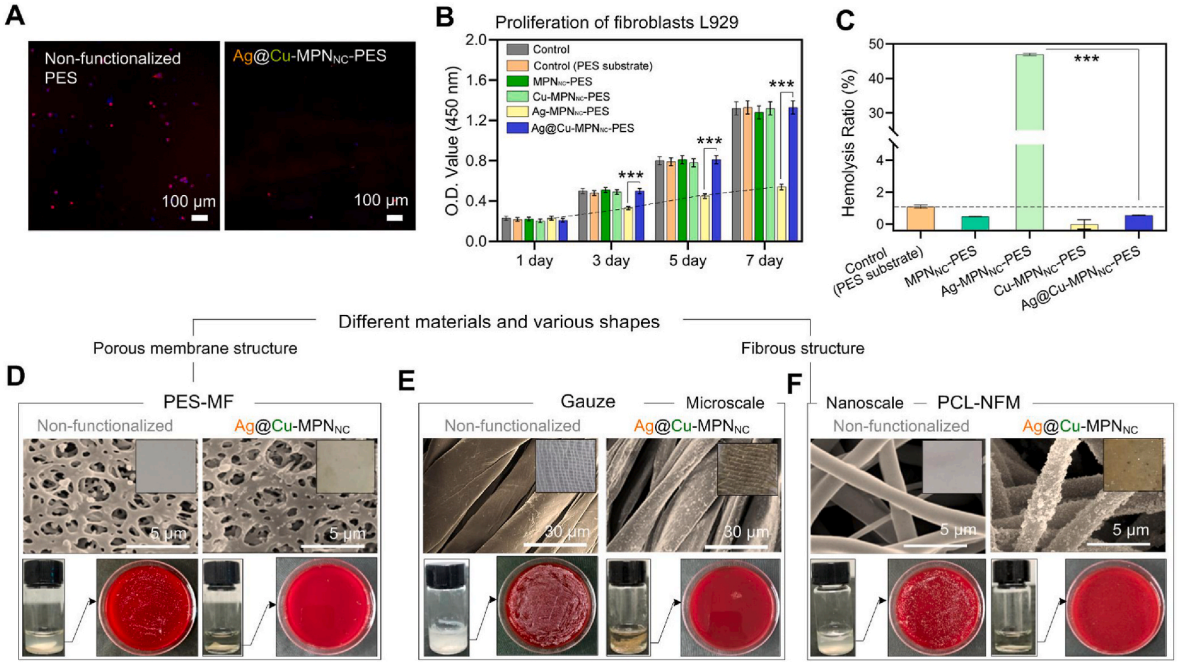

Fig. 5. Cell toxicity and surface-functionalization of different substrates. (A) Representative fluorescence microscopy images for pristine PES and Ag@Cu-MPN$_{NC}$-PES after being cultured with L929 cells (mouse fibroblasts) for 24h. The lower density of cells indicates the low-fouling property after the functionalization of Ag@Cu-MPN$_{NC}$. (B) Cell density of L929 cells (profiled by using a CCK-8 assay at OD$_{450}$) at different days with the incubation of different membranes. The cell density of the group treated with Ag@Cu-MPN$_{NC}$-PES shows a significant difference compared with Ag-MPN$_{NC}$, due to the dramatic decrease of the cytotoxicity of alloyed nanostructure compared with only Ag-based coating. (C) Hemolysis ratios of human red bloods cells (RBCs) after the incubation with different membranes for 3h. The hemolysis ratio of the group treated with Ag@Cu-MPN$_{NC}$-PES shows significantly lower value compared with Ag-MPN$_{NC}$-PES and no difference compared with the bare PES group. Variation is represented by SE (error bars) from three independent replicates for all data points, *** (p-value < 0.05). (D–F) Demonstration of substrate-independent functionalization of Ag@Cu-MPN$_{NC}$ on clinically used materials. The SEM images show the microstructure of the membranes before and after Ag@Cu-MPN$_{NC}$ functionalization (upper panel, PES-MF, Gauze, and PCL-NFM). The insets show the visual change of the membranes. The bottom-left panels show the photographs of the supernatants incubated with different membranes. Cloudiness demonstrates the presence of bacteria in suspension after 16 h-incubation. The bottom-right panels show representative photographs of bacterial colonies formed on SBA plates treated with different control and functionalized membranes. No colonies can be observed on the group treated with Ag@Cu-MPN$_{NC}$-functionalized membranes.

antibacterial properties. Due to the ease of functionalization process and the low cost of natural polyphenols, this platform could significantly reduce the cost of fabrication and broaden the choice of substrates used in wound healing [89], which is important for future large-scale manufacturing and clinical applications [69]. Moreover, this allowed us to explore the in vivo application of Ag@Cu-MPN$_{NC}$.

3.4. Ag@Cu-MPN$_{NC}$ for full-thickness skin wound healing

The superior antibacterial ability and biocompatibility encouraged us to explore the application of the Ag@Cu-MPN$_{NC}$ for wound disinfection and healing in vivo. PCL-NFM was chosen as the model substrate due to its wide use in clinic for a variety of applications. A wound was firstly created on the back of shaved Sprague Dawley (SD) rats, followed by incubation with *S. aureus*, and finally treated with Ag@Cu-MPN$_{NC}$-functionalized NFM or control groups (PBS, bare NFM, MPN$_{NC}$-, and Ag-MPN$_{NC}$-functionalized NFM) (Fig. 6A). The wounds were photographed at 0, 2, 6, 10, and 14 days after the treatments, and notably the size of the wound tended to decrease quickly for the Ag@Cu-MPN$_{NC}$ group at each observed time point, and the wound areas were significantly smaller than other groups (Fig. 6B). The wounds were photographed 0, 2, 6, 10, and 14 days after treatments, and notably the size of the wound tended to decrease quickly for the Ag@Cu-MPN$_{NC}$ group at each observed time point, and the wound areas were significantly smaller than other groups (Fig. 6B). The wound areas were measured precisely to determine the wound closure efficiency [1,38,45]. After 14 day-treatment, the Ag@Cu-MPN$_{NC}$-functionalized NFM treated group showed a wound-healing ratio of nearly 100%, indicating an efficient disinfection effect and accelerated wound healing process compared (Fig. 6C). Meanwhile, after 14 days, the corresponding values of the CFU for *S. aureus* from the wounds were counted, and barely any colonies could be seen in the Ag@Cu-MPN$_{NC}$-functionalized NFM treated groups.

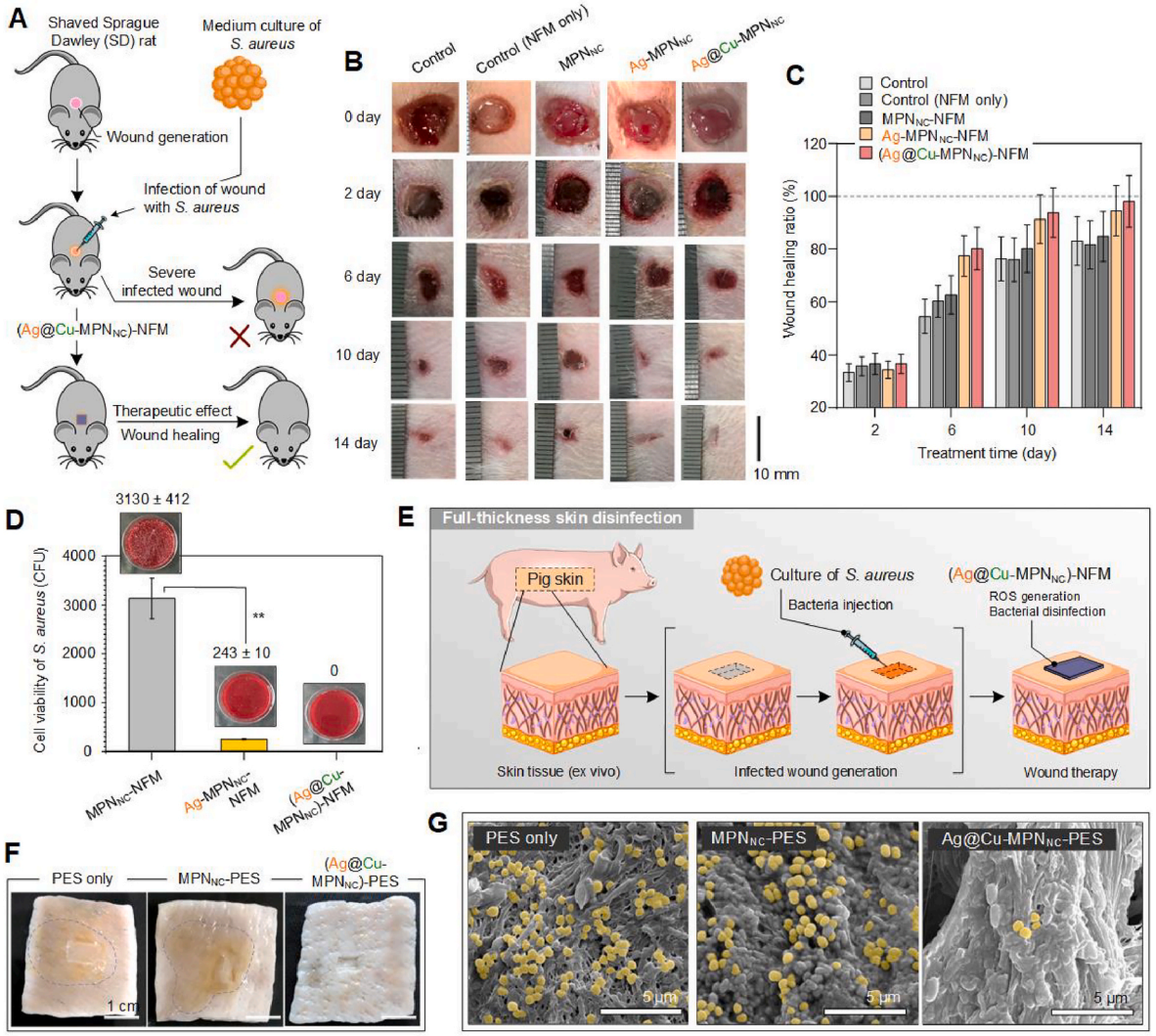

Fig. 6. Wound disinfection and the promoted healing effects of Ag@Cu-MPN$_{NC}$. (A) Schematic of *S. aureus*-based wound infection in SD rat model and the treatment by Ag@Cu-MPN$_{NC}$. (B) Representative photographs of the wounds in the rats at different time intervals during the therapeutic process. Different control groups were compared against Ag@Cu-MPN$_{NC}$. (C) Statistic wound healing ratios for the different treatment groups, in which the alloyed nanostructured Ag@Cu-MPN$_{NC}$-treated group showed the highest wound healing ratio after 6 days of treatment. (D) Living cell numbers of *S. aureus* in the wound areas treated with different materials. The cell viability was counted from the SBA plates. The bacterial numbers of Ag@Cu-MPN$_{NC}$ and Ag-MPN$_{NC}$ were both significantly lower than that of PCL-NFM membrane, which was only functionalized by an MPN$_{NC}$ (Fe^{III}-TA) layer. (E) Ag@Cu-MPN$_{NC}$-induced generation of anti-inflammatory factors. The presence of alloyed nanostructure on the MPN coating promotes the wound healing by disinfection and by lowering the inflammation. (F) Schematic of *S. aureus* wound infection on full-thickness skin tissue from pig. (G) Photographs of the *S. aureus* wound infection on pig skin tissues treated with different materials. Purple dashed lines indicate the presence of *S. aureus* on the wounds (yellow areas). (H) SEM images of the microstructures of wounds treated with different materials. The number of *S. aureus* was dramatically lower than those of the groups treated with PES and MPN$_{NC}$-coated PES membranes. *S. aureus* cells were false-colored in yellow.

These results further confirmed the significant antibacterial effect against *S. aureus* after the 14-day treatment for the Ag@Cu-MPN_{NC}--functionalized NFM (Fig. 6D).

The disinfection effect of the Ag@Cu-MPN_{NC} was further evaluated based on an infectious full-thickness pig skin model. Pig skin shows physiological similarities in both structure and composition to those of human skin tissue. Therefore, the three-dimensional fibrous structure and its tissue microenvironment could better mimic the therapeutic effect of Ag@Cu-MPN_{NC} on human skin. In this experiment, the skin was first wounded and infected by *S. aureus*, and then Ag@Cu-MPN_{NC}-NFM was used to dress the wounds (Fig. 6E). After 3 days incubation, photographs of the pig skins treated with bare PES and MPN_{NC} showed large areas of infection compared to the Ag@Cu-MPN_{NC}-dressed wounds, which showed no visible infection (Fig. 6F). Meanwhile, the micromorphologies of the skins were observed by SEM for further evaluation. The skin samples with visible infection showed a large number of bacteria embedded on the surface of the fibrous skin tissue (Fig. 6G). However, for the Ag@Cu-MPN_{NC}-dressed wounds, bacterial adhesion was minimal and the number of bacteria was much less than that on the infected skin samples. These results strongly supported that the bacterial growth on the pig skin was significantly inhibited by the Ag@Cu-MPN_{NC}, and demonstrated great promise for further clinical use.

To further evaluate the tissue microstructure changes during the wound healing, histological characterization of the wounds at day 14 was conducted by the hematoxylin-eosin (H&E) staining method [18, 28]. An abnormal pathway was used for the tissue regeneration process of control groups, as non-intact epidermal layers and loose connective dermis structures could be seen for the samples treated with NFM and MPN_{NC}-NFM (Fig. S11). In contrast, an intact epidermal layer and fully recovered dermis structure were observed in the tissue sample treated with Ag@Cu-MPN_{NC}-NFM. More importantly, regenerated blood vessels filled with red blood cells were clearly observed from the Ag@Cu-MPN_{NC} treated wound (Fig. 7A). These imaging results demonstrated that the Ag@Cu-MPN_{NC} performed synergistic therapeutic effects with the combination of enhanced bacterial disinfection activity and revascularization. Additionally, immunohistochemical staining based on vascular endothelial growth factor (VEGF) was also performed at 14-day post-treatment to verify the formation of the

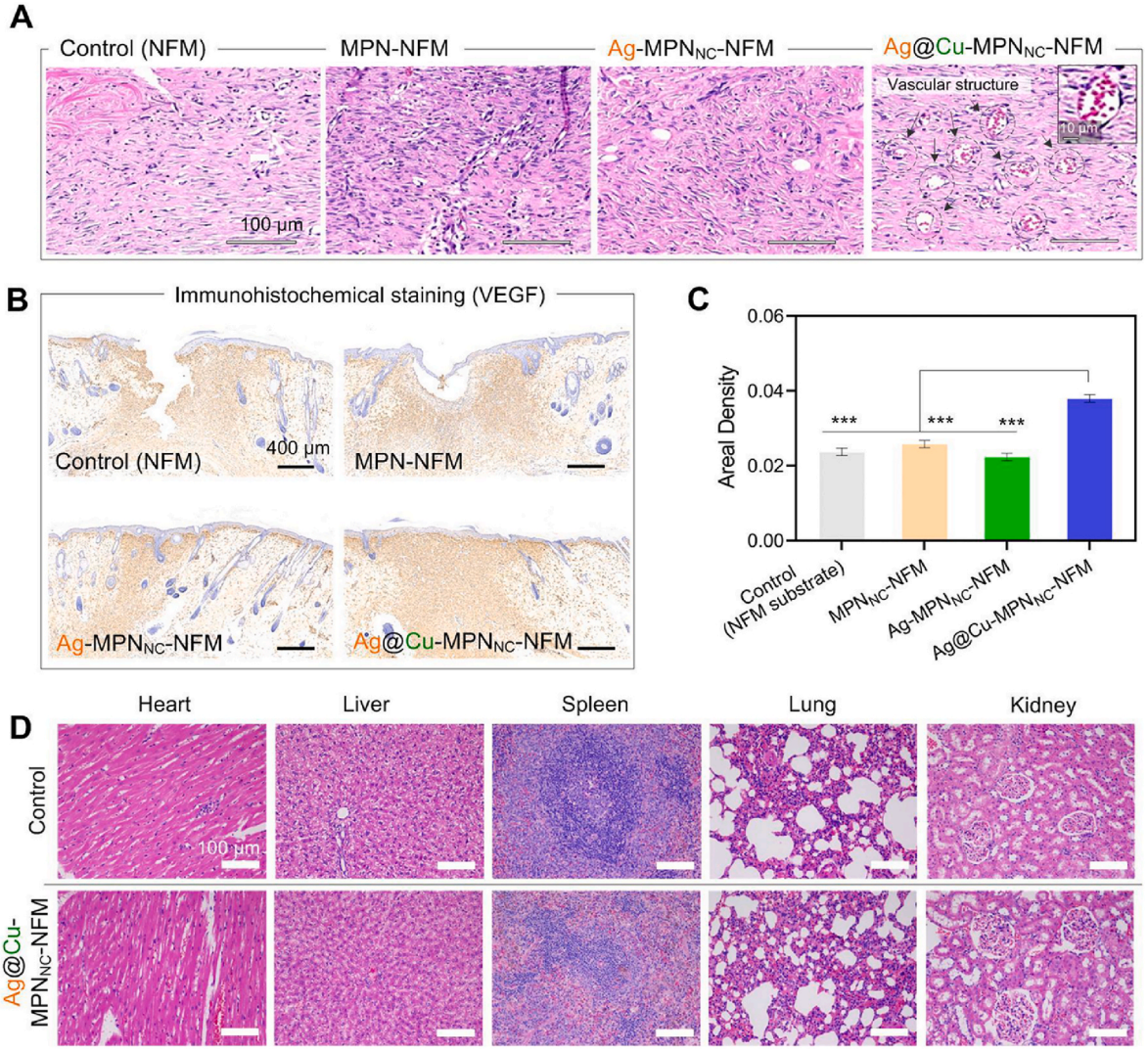

Fig. 7. Promoted revascularization of wound tissue and in vivo toxicity of Ag@Cu-MPN_{NC}. (A) H&E stained histological sections show the formed epithelium after the treatment with different dressings. Red arrows highlight the regeneration of blood vessels in the wound tissues when treated with *Ag@Cu-MPN_{NC}-NFM*. (B) Immunohistochemical (VEGF) stained histological sections show the regeneration of vascular microstructures after the treatment with different dressings. (C) Statistic vascular regeneration ratios in the different dressing groups. The tissue treated with Ag@Cu-MPN_{NC} showed a significantly higher VEGF staining density than the other groups. The variation is represented by the standard deviation of three independent replicates in all graphs, *** (p-value < 0.05). (D) Histopathology of the heart, liver, and kidney from the rats. The main organs were collected and processed for histological analysis. The sections were stained with H&E. Images are representative of three independent experiments.

regenerated blood vessels (Fig. 7B). The significantly higher staining density value indicated the increase of VEGF expression in the tissue treated with Ag@Cu-MPN$_{NC}$, which effectively promoted wound healing (Fig. 7C). The Cu would decompose the endogenous S-nitrosothiols in the blood generating nitric oxide [90], which can promote angiogenesis and wound healing. Histological evaluation of the treated rats was carried out to examine whether there was any damage to the main organs including heart, liver, spleen, lung and kidney during the application of Ag@Cu-MPN$_{NC}$ (Fig. 7D). The results showed that there were no obvious anomalies in the Ag@Cu-MPN$_{NC}$-treated group in comparison with the control group [3]. Our results suggest that this naturally-derived MPN system provides a novel and safe platform for the engineering of alloyed nanostructures which significantly promotes the generation of the critically needed vascular system during wound healing.

4. Conclusions

In summary, we present a nanoplatform for the functionalization of a variety of medical substrates for synergistic wound disinfection and vascular regeneration. The modular nature and chemistry of MPNs allows for the synthesis of bimetallic alloyed Ag@Cu nanostructures on medical substrates through a spontaneous co-reduction and disproportionation reaction of the incorporated metal ions. The universally-adherent nature of MPNs allowed the Ag@Cu-MPN$_{NC}$ to endow a wide range of medical substrates with synergistic therapeutic effects. We confirmed that the Ag@Cu-MPN$_{NC}$ exhibited superior antibacterial ability against both Gram-positive and Gram-negative bacteria over its monometallic counterpart. Furthermore, our mechanistic studies revealed that an elevated level of ROS could be generated by the Cu domain of the alloyed nanostructures, while the Ag domain could simultaneously cause the disruption of cell membranes, leading to the efficient penetration of ROS into the cytosol and the oxidization of intracellular proteins. More importantly, the Ag@Cu-MPN$_{NC}$ showed a combination of therapeutic functions to inhibit the bacterial invasion and modulate various bio-nano interactions leading to tissue repair. Rat and pig infected models proved the outstanding antimicrobial performance of the Ag@Cu-MPN$_{NC}$ against *S. aureus*. Moreover, quantified wound healing values and histological studies demonstrated the accelerated wound closure performance and the excellent revascularization of the injured tissue with no obvious systemic toxicity. We believe that this rapid and efficient nanoplatform presents great potential for coating medical devices, wound dressings, and artificial implants, in a simple, cost-effective, and scalable manner.

Data availability

All of the data reported in this work as available upon request.

CRediT authorship contribution statement

Yi Xie: Investigation, Methodology, Data curation, Writing – original draft, Funding acquisition. **Shengqiu Chen:** Investigation, Methodology, Data curation, Visualization. **Xu Peng:** Investigation, Data curation. **Xiaoling Wang:** Data curation, Investigation, Formal analysis, Software. **Zhiwei Wei:** Data curation, Investigation. **Joseph J. Richardson:** Data curation, Software. **Kang Liang:** Software, Visualization, Data curation. **Hirotaka Ejima:** Investigation, Formal analysis. **Junling Guo:** Conceptualization, Supervision, Methodology, Software, Writing – review & editing. **Changsheng Zhao:** Conceptualization, Supervision, Funding acquisition, Writing – review & editing.

Declaration of competing interest

The authors declare that they have no known competing financial interests or personal relationships that could have appeared to influence the work reported in this paper.

Acknowledgements

This work was supported by the National Natural Science Foundation of China (Grant No. 51903168, 51673125, and 51873115), State Key Research Development Programme of China (Grant Nos. 2016YFC1103000 and 2018YFC1106400), International Visiting Program for Excellent Young Scholars of Sichuan University, and the China Postdoctoral Science Foundation (2018M643485). The work in the J.G. laboratory was financially supported by the National Global Talents Recruitment Program (J.G.), National Natural Science Foundation of China (J.G., Grant No.22178233) State Key Laboratory of Polymer Materials Engineering (J.G., Grant No. sklpme2020-3-01), Double First Class University Plan (J.G.), Key Laboratory of Leather Chemistry and Engineering (J.G.), and National Engineering Research Center of Clean Technology in Leather Industry (J.G.). We also gratefully acknowledge the help of Hui Wang for SEM observation.

Appendix A. Supplementary data

Supplementary data to this article can be found online at https://doi.org/10.1016/j.bioactmat.2022.03.004.

References

[1] B. Xu, H. Wang, W. Wang, L. Gao, S. Li, X. Pan, H. Wang, H. Yang, X. Meng, Q. Wu, A single-atom nanozyme for wound disinfection applications, Angew. Chem. Int. Ed. 58 (2019) 4911–4916.
[2] Y. Zhang, P. Sun, L. Zhang, Z. Wang, F. Wang, K. Dong, Z. Liu, J. Ren, X. Qu, Silver-infused porphyrinic metal-organic framework: surface-adaptive, on-demand nanoplatform for synergistic bacteria killing and wound disinfection, Adv. Funct. Mater. 29 (2019), 1808594.
[3] X. Yao, G. Zhu, P. Zhu, J. Ma, W. Chen, Z. Liu, T. Kong, Omniphobic ZIF-8@ hydrogel membrane by microfluidic-emulsion-templating method for wound healing, Adv. Funct. Mater. 30 (2020), 1909389.
[4] X. Zeng, D.T. McCarthy, A. Deletic, X. Zhang, Silver/reduced graphene oxide hydrogel as novel bactericidal filter for point-of-use water disinfection, Adv. Funct. Mater. 25 (2015) 4344–4351.
[5] S. Hamdan, I. Pastar, S. Drakulich, E. Dikici, M. Tomic-Canic, S. Deo, S. Daunert, Nanotechnology-driven therapeutic interventions in wound healing: potential uses and applications, ACS Cent. Sci. 3 (2017) 163–175.
[6] G. Chen, Y. Yu, X. Wu, G. Wang, J. Ren, Y. Zhao, Bioinspired multifunctional hybrid hydrogel promotes wound healing, Adv. Funct. Mater. 28 (2018), 1801386.
[7] X. Zhang, G. Chen, Y. Liu, L. Sun, L. Sun, Y. Zhao, Black phosphorus-loaded separable microneedles as responsive oxygen delivery carriers for wound healing, ACS Nano 14 (2020) 5901–5908.
[8] M. Wang, C. Wang, M. Chen, Y. Xi, W. Cheng, C. Mao, T. Xu, X. Zhang, C. Lin, W. Gao, Y. Guo, B. Lei, Efficient angiogenesis-based diabetic wound healing/skin reconstruction through bioactive antibacterial adhesive ultraviolet shielding nanodressing with exosome release, ACS Nano 13 (2019) 10279–10293.
[9] Y. Xi, J. Ge, Y. Guo, B. Lei, P. Ma, Biomimetic elastomeric polypeptide-based nanofibrous matrix for overcoming multidrug-resistant bacteria and enhancing full-thickness wound healing/skin regeneration, ACS Nano 12 (2018) 10772–10784.
[10] C. Mao, Y. Xiang, X. Liu, Z. Cui, X. Yang, K. Yeung, H. Pan, X. Wang, P. Chu, S. Wu, Photo-inspired antibacterial activity and wound healing acceleration by hydrogel embedded with Ag/Ag@ AgCl/ZnO nanostructures, ACS Nano 11 (2017) 9010–9021.
[11] S. Castleberry, B. Almquist, W. Reis, J. Chow, S. Mayner, P. Hammond, Self-assembled wound dressings silence MMP-9 and improve diabetic wound healing in vivo, Adv. Mater. 28 (2016) 1809–1817.
[12] A. Boddupalli, L. Zhu, K. Bratlie, Methods for implant acceptance and wound healing: material selection and implant location modulate macrophage and fibroblast phenotypes, Adv. Healthc. Mater. 5 (2016) 2575–2594.
[13] Z. Meng, D. Zhou, Y. Gao, M. Zeng, W. Wang, miRNA delivery for skin wound healing, Adv. Drug Deliv. Rev. 129 (2018) 308–318.
[14] A. Lisovsky, M. Chamberlain, L. Wells, M. Sefton, Cell interactions with vascular regenerative MAA-based materials in the context of wound healing, Adv. Healthc. Mater. 4 (2015) 2375–2387.
[15] X. Xie, T. Sun, J. Xue, Z. Miao, X. Yan, W. Fang, Q. Li, R. Tang, Y. Lu, L. Tang, Ag nanoparticles cluster with pH-triggered reassembly in targeting antimicrobial applications, Adv. Funct. Mater. 30 (2020) 2000511.
[16] K. Stapelfeldt, S. Stamboroski, I. Walter, N. Suter, T. Kowalik, M. Michaelis, D. Brüggemann, Controlling the multiscale structure of nanofibrous fibrinogen scaffolds for wound healing, Nano Lett. 19 (2019) 6554–6563.
[17] M.A.M. Jahromi, P.S. Zangabad, S. Basri, K. Zangabad, A. Ghamarypour, A. Aref, M. Karimi, M.R. Hamblin, Nanomedicine and advanced technologies for burns:

preventing infection and facilitating wound healing, Adv. Drug Deliv. Rev. 123 (2018) 33–64.
[18] Z. Fan, B. Liu, J. Wang, S. Zhang, Q. Lin, P. Gong, L. Ma, S. Yang, A novel wound dressing based on Ag/graphene polymer hydrogel: effectively kill bacteria and accelerate wound healing, Adv. Funct. Mater. 24 (2014) 3933–3943.
[19] X. Hu, L. Chu, X. Dong, G. Chen, T. Tang, D. Chen, X. He, H. Tian, Multivalent glycosheets for double light-driven therapy of multidrug-resistant bacteria on wounds, Adv. Funct. Mater. 29 (2019) 1806986.
[20] J. Zhou, D. Yao, Z. Qian, S. Hou, L. Li, A.T.A. Jenkins, Y. Fan, Bacteria-responsive intelligent wound dressing: simultaneous in situ detection and inhibition of bacterial infection for accelerated wound healing, Biomaterials 161 (2018) 11–23.
[21] A. Breij, M. Riool, R.A. Cordfunke, N. Malanovic, L. Boer, R.I. Koning, E. Ravensbergen, M. Franken, T. Heijde, B.K. Boekema, The antimicrobial peptide SAAP-148 combats drug-resistant bacteria and biofilms, Sci. Transl. Med. 10 (2018), eaan4044.
[22] J. Deng, Y. Tang, Q. Zhang, C. Wang, M. Liao, P. Ji, J. Song, G. Luo, L. Chen, X. Ran, A bioinspired medical adhesive derived from skin secretion of andrias davidianus for wound healing, Adv. Funct. Mater. 29 (2019) 1809110.
[23] X. Zhao, Y. Liang, Y. Huang, J. He, Y. Han, B. Guo, Physical double-network hydrogel adhesives with rapid shape adaptability, fast self-healing, antioxidant and NIR/pH stimulus-responsiveness for multidrug-resistant bacterial infection and removable wound dressing, Adv. Funct. Mater. 30 (2020) 1910748.
[24] Y. Li, Z. Zhao, J. Zhang, R.T. Kwok, S. Xie, R. Tang, Y. Jia, J. Yang, L. Wang, J. W. Lam, W. Zheng, X. Jiang, B. Zhong, A bifunctional aggregation-induced emission luminogen for monitoring and killing of multidrug-resistant bacteria, Adv. Funct. Mater. 28 (2018) 1804632.
[25] L. Huang, J. Chen, L. Gan, J. Wang, S. Dong, Single-atom nanozymes, Sci. Adv. 5 (2019), eaav5490.
[26] Y. Huang, J. Ren, X. Qu, Nanozymes: classification, catalytic mechanisms, activity regulation, and applications, Chem. Rev. 119 (2019) 4357–4412.
[27] F. Cao, L. Zhang, H. Wang, Y. You, Y. Wang, N. Gao, J. Ren, X. Qu, Defect-rich adhesive nanozymes as efficient antibiotics for enhanced bacterial inhibition, Angew. Chem. Int. Ed. 58 (2019) 16236–16242.
[28] C. Ge, R. Wu, Y. Chong, G. Fang, X. Jiang, Y. Pan, C. Chen, J. Yin, Synthesis of Pt hollow nanodendrites with enhanced peroxidase-like activity against bacterial infections: implication for wound healing, Adv. Funct. Mater. 28 (2018) 1801484.
[29] M. Eshed, J. Lellouche, A. Gedanken, E. Banin, A Zn-doped CuO nanocomposite shows enhanced antibiofilm and antibacterial activities against streptococcus mutans compared to nanosized CuO, Adv. Funct. Mater. 24 (2014) 1382–1390.
[30] P. Leidinger, J. Treptow, K. Hagens, J. Eich, N. Zehethofer, D. Schwudke, W. Oehlmann, H. Lünsdorf, O. Goldmann, U.E. Schaible, Isoniazid@Fe_2O_3 nanocontainers and their antibacterial effect on tuberculosis mycobacteria, Angew. Chem. Int. Ed. 54 (2015) 12597–12601.
[31] K. Rasool, M. Helal, A. Ali, C.E. Ren, Y. Gogotsi, K.A. Mahmoud, Antibacterial activity of $Ti_3C_2T_x$ MXene, ACS Nano 10 (2016) 3674–3684.
[32] Y.H. Leung, A.M. Ng, X. Xu, Z. Shen, L.A. Gethings, M.T. Wong, C.M. Chan, M. Y. Guo, Y.H. Ng, A.B. Djurišić, Mechanisms of antibacterial activity of MgO: non-ROS mediated toxicity of MgO nanoparticles towards *Escherichia coli*, Small 10 (2014) 1171–1183.
[33] Y. Zhao, Q. Cai, W. Qi, Y. Jia, T. Xiong, Z. Fan, S. Liu, J. Yang, N. Li, B. Chang, BSA-CuS nanoparticles for photothermal therapy of diabetic wound infection in vivo, ChemistrySelect 3 (2018) 9510–9516.
[34] W. Wang, C. Hao, M. Sun, L. Xu, X. Wu, C. Xu, H. Kuang, Peptide mediated chiral inorganic nanomaterials for combating gram-negative bacteria, Adv. Funct. Mater. 28 (2018) 1805112.
[35] Y. Yang, L. Ma, C. Cheng, Y. Deng, J. Huang, X. Fan, C. Nie, W. Zhao, C. Zhao, Nonchemotherapic and robust dual-responsive nanoagents with on-demand bacterial trapping, ablation, and release for efficient wound disinfection, Adv. Funct. Mater. 28 (2018) 1705708.
[36] S.H. Bhang, W.S. Jang, J. Han, J.K. Yoon, W.G. La, E. Lee, Y.S. Kim, J.Y. Shin, T. J. Lee, H.K. Baik, Zinc oxide nanorod-based piezoelectric dermal patch for wound healing, Adv. Funct. Mater. 27 (2017) 1603497.
[37] D. Mao, F. Hu, S. Ji, W. Wu, D. Ding, D. Kong, B. Liu, Metal-organic-framework-assisted in vivo bacterial metabolic labeling and precise antibacterial therapy, Adv. Mater. 30 (2018) 1706831.
[38] K. Lu, C. He, N. Guo, C. Chan, K. Ni, G. Lan, H. Tang, C. Pelizzari, Y. Fu, M. T. Spiotto, Low-dose X-ray radiotherapy-radiodynamic therapy via nanoscale metal-organic frameworks enhances checkpoint blockade immunotherapy, Nat. Biomed. Eng. 2 (2018) 600.
[39] W. Liu, J. Li, M. Cheng, Q. Wang, Y. Qian, K.W. Yeung, P.K. Chu, X. Zhang, A surface-engineered polyetheretherketone biomaterial implant with direct and immunoregulatory antibacterial activity against methicillin-resistant Staphylococcus aureus, Biomaterials 208 (2019) 8–20.
[40] S. Yan, S. Chen, X. Gou, J. Yang, J. An, X. Jin, Y.W. Yang, L. Chen, H. Gao, Biodegradable supramolecular materials based on cationic polyaspartamides and pillar[5]arene for targeting gram-positive bacteria and mitigating antimicrobial resistance, Adv. Funct. Mater. 29 (2019) 1904683.
[41] S.J. Lam, N.M. O'Brien-Simpson, N. Pantarat, A. Sulistio, E.H. Wong, Y. Chen, J. C. Lenzo, J.A. Holden, A. Blencowe, E.C. Reynolds, Combating multidrug-resistant gram-negative bacteria with structurally nanoengineered antimicrobial peptide polymers, Nat. Microbio. 1 (2016) 1–11.
[42] J. Li, Z. Chen, M. Zhou, J. Jing, W. Li, Y. Wang, L. Wu, L. Wang, Y. Wang, M. Lee, Polyoxometalate-driven self-assembly of short peptides into multivalent nanofibers with enhanced antibacterial activity, Angew. Chem. Int. Ed. 55 (2016) 2592–2595.
[43] M.D. Konieczynska, J.C. Villa-Camacho, C. Ghobril, M. Perez-Viloria, K.M. Tevis, W.A. Blessing, A. Nazarian, E.K. Rodriguez, M.W. Grinstaff, On-demand dissolution of a dendritic hydrogel-based dressing for second-degree burn wounds through thiol-thioester exchange reaction, Angew. Chem. Int. Ed. 55 (2016) 9984–9987.
[44] R. Nudelman, H. Alhmoud, B. Delalat, S. Fleicher, E. Fine, T. Guliakhmedova, R. Elnathan, A. Nyska, N.H. Voelcker, M. Gozin, Jellyfish-based smart wound dressing devices containing in situ synthesized antibacterial nanoparticles, Adv. Funct. Mater. 29 (2019) 1902783.
[45] T. Cramer, I. Fratelli, P. Barquinha, A. Santa, C. Fernandes, F. D'Annunzio, C. Loussert, R. Martins, E. Fortunato, B. Fraboni, Passive radiofrequency x-ray dosimeter tag based on flexible radiation-sensitive oxide field-effect transistor, Sci. Adv. 4 (2018), eaat1825.
[46] J. Li, R. Cha, K. Mou, X. Zhao, K. Long, H. Luo, F. Zhou, X. Jiang, Nanocellulose-based antibacterial materials, Adv. Healthc. Mater. 7 (2018) 1800334.
[47] Z. Chen, H. Ji, C. Liu, W. Bing, Z. Wang, X. Qu, A multinuclear metal complex based DNase-mimetic artificial enzyme: matrix cleavage for combating bacterial biofilms, Angew. Chem. Int. Ed. 55 (2016) 10732–10736.
[48] H. Bai, H. Yuan, C. Nie, B. Wang, F. Lv, L. Liu, S. Wang, A supramolecular antibiotic switch for antibacterial regulation, Angew. Chem. Int. Ed. 54 (2015) 13208–13213.
[49] N. Huang, X. Chen, X. Zhu, M. Xu, J. Liu, Ruthenium complexes/polypeptide self-assembled nanoparticles for identification of bacterial infection and targeted antibacterial research, Biomaterials 141 (2017) 296–313.
[50] Z. Yu, X. Li, F. Xu, X. Hu, J. Yan, N. Kwon, G. Chen, T. Tang, X. Dong, Y. Mai, Degradation of structurally defined graphene nanoribbons by myeloperoxidase and the photo-fenton reaction, Angew. Chem. Int. Ed. 132 (2020) 3687–3693.
[51] Y. Tao, E. Ju, J. Ren, X. Qu, Bifunctionalized mesoporous silica-supported gold nanoparticles: intrinsic oxidase and peroxidase catalytic activities for antibacterial applications, Adv. Mater. 27 (2015) 1097–1104.
[52] G. Fang, W. Li, X. Shen, J.M. Perez-Aguilar, Y. Chong, X. Gao, Z. Chai, C. Chen, C. Ge, R. Zhou, Differential Pd-nanocrystal facets demonstrate distinct antibacterial activity against gram-positive and gram-negative bacteria, Nat. Commun. 9 (2018) 1–9.
[53] W.C. Hu, M.R. Younis, Y. Zhou, C. Wang, X. Xia, In situ fabrication of ultrasmall gold nanoparticles/2D MOFs hybrid as nanozyme for antibacterial therapy, Small 16 (2020) 2000553.
[54] B. Le Ouay, F. Stellacci, Antibacterial activity of silver nanoparticles: a surface science insight, Nano Today 10 (2015) 339–354.
[55] Z. Wang, K. Dong, Z. Liu, Y. Zhang, Z. Chen, H. Sun, J. Ren, X. Qu, Activation of biologically relevant levels of reactive oxygen species by Au/g-C_3N_4 hybrid nanozyme for bacteria killing and wound disinfection, Biomaterials 113 (2017) 145–157.
[56] A.P. Richter, J.S. Brown, B. Bharti, A. Wang, S. Gangwal, K. Houck, E.A.C. Hubal, V.N. Paunov, S.D. Stoyanov, O.D. Velev, An environmentally benign antimicrobial nanoparticle based on a silver-infused lignin core, Nat. Nanotechnol. 10 (2015) 817.
[57] Y. Zhao, C. Ye, W. Liu, R. Chen, X. Jiang, Tuning the composition of AuPt bimetallic nanoparticles for antibacterial application, Angew. Chem. Int. Ed. 53 (2014) 8127–8131.
[58] H. Qin, Y. Zhao, Z. An, M. Cheng, Q. Wang, T. Cheng, Q. Wang, J. Wang, Y. Jiang, X. Zhang, Enhanced antibacterial properties, biocompatibility, and corrosion resistance of degradable Mg-Nd-Zn-Zr alloy, Biomaterials 53 (2015) 211–220.
[59] Y. Li, L. Liu, P. Wan, Z. Zhai, Z. Mao, Z. Ouyang, D. Yu, Q. Sun, L. Tan, L. Ren, Biodegradable Mg-Cu alloy implants with antibacterial activity for the treatment of osteomyelitis: in vitro and in vivo evaluations, Biomaterials 106 (2016) 250–263.
[60] M. Li, Z. Ma, Y. Zhu, H. Xia, M. Yao, X. Chu, X. Wang, K. Yang, M. Yang, Y. Zhang, Toward a molecular understanding of the antibacterial mechanism of copper-bearing titanium alloys against *Staphylococcus aureus*, Adv. Healthc. Mater. 5 (2016) 557–566.
[61] P. Sotoudehbagha, S. Sheibani, M. Khakbiz, S. Ebrahimi-Barough, H. Hermawan, Novel antibacterial biodegradable Fe-Mn-Ag alloys produced by mechanical alloying, Mater. Sci. Eng. C 88 (2018) 88–94.
[62] L. Yang, L. Chen, Y. Chen, L. Kang, J. Yu, Y. Wang, C. Lu, T. Mashimo, A. Yoshiasa, C. Lin, Homogeneously alloyed nanoparticles of immiscible Ag-Cu with ultrahigh antibacterial activity, Colloids Surf. B Biointerfaces 180 (2019) 466–472.
[63] Z. Gao, M. Song, R. Liu, Y. Shen, L. Ward, I. Cole, X. Chen, X. Liu, Improving in vitro and in vivo antibacterial functionality of Mg alloys through micro-alloying with Sr and Ga, Mater. Sci. Eng. C 104 (2019) 109926.
[64] A. Ahmad, L. Li, J. Bao, X. Jia, Y. Xu, X. Guo, Antibacterial activity of graphene supported FeAg bimetallic nanocomposites, Colloids Surf. B Biointerfaces 143 (2016) 490–498.
[65] I. Carvalho, N. Dias, M. Henriques, S. Calderon V, P. Ferreira, A. Cavaleiro, S. Carvalho, Antibacterial effects of bimetallic clusters incorporated in amorphous carbon for stent application, ACS Appl. Mater. Interfaces 12 (2020) 24555–24563.
[66] Y. Liu, H. Meng, Z. Qian, N. Fan, W. Choi, F. Zhao, B.P. Lee, A moldable nanocomposite hydrogel composed of a mussel-inspired polymer and a nanosilicate as a fit-to-shape tissue sealant, Angew. Chem. Int. Ed. 129 (2017) 4288–4292.
[67] S. Chigurupati, M.R. Mughal, E. Okun, S. Das, A. Kumar, M. McCaffery, S. Seal, M. P. Mattson, Effects of cerium oxide nanoparticles on the growth of keratinocytes, fibroblasts and vascular endothelial cells in cutaneous wound healing, Biomaterials 34 (2013) 2194–2201.
[68] S. Yu, G. Li, P. Zhao, Q. Cheng, Q. He, D. Ma, W. Xue, NIR-laser-controlled hydrogen-releasing pdh nanohydride for synergistic hydrogen-photothermal antibacterial and wound-healing therapies, Adv. Funct. Mater. 29 (2019) 1905697.
[69] H. Ejima, J.J. Richardson, F. Caruso, Metal-phenolic networks as a versatile platform to engineer nanomaterials and biointerfaces, Nano Today 12 (2017) 136–148.

[70] J. Guo, Y. Ping, H. Ejima, K. Alt, M. Meissner, J.J. Richardson, Y. Yan, K. Peter, D. Von Elverfeldt, C.E. Hagemeyer, F. Caruso, Engineering multifunctional capsules through the assembly of metal-phenolic networks, Angew. Chem. Int. Ed. 53 (2014) 5546–5551.
[71] K. Li, G. Xiao, J.J. Richardson, B.L. Tardy, H. Ejima, W. Huang, J. Guo, X. Liao, B. Shi, Targeted therapy against metastatic melanoma based on self-assembled metal-phenolic nanocomplexes comprised of green tea catechin, Adv. Sci. 6 (2019) 1801688.
[72] W. Luo, G. Xiao, F. Tian, J.J. Richardson, Y. Wang, J. Zhou, J. Guo, X. Liao, B. Shi, Engineering robust metal-phenolic network membranes for uranium extraction from seawater, Energy Environ. Sci. 12 (2019) 607–614.
[73] J. Guo, B.L. Tardy, A.J. Christofferson, Y. Dai, J.J. Richardson, W. Zhu, M. Hu, Y. Ju, J. Cui, R.R. Dagastine, Modular assembly of superstructures from polyphenol-functionalized building blocks, Nat. Nanotechnol. 11 (2016) 1105.
[74] W. Chen, Y. Cai, Q. Fu, B. Chen, J. Guo, J.J. Chou, Unidirectional presentation of membrane proteins in nanoparticle-supported liposomes, Angew. Chem. Int. Ed. 58 (2019) 9866–9870.
[75] H. Ejima, J.J. Richardson, K. Liang, J.P. Best, M.P. van Koeverden, G.K. Such, J. Cui, F. Caruso, One-step assembly of coordination complexes for versatile film and particle engineering, Science 341 (2013) 154–157.
[76] L. Mi, S. Jiang, Integrated antimicrobial and nonfouling zwitterionic polymers, Angew. Chem. Int. Ed. 53 (2014) 1746–1754.
[77] Y. Zhu, J. Zhang, J. Song, J. Yang, Z. Du, W. Zhao, H. Guo, C. Wen, Q. Li, X. Sui, A multifunctional pro-healing zwitterionic hydrogel for simultaneous optical monitoring of pH and glucose in diabetic wound treatment, Adv. Funct. Mater. 30 (2020) 1905493.
[78] G. Yun, S. Pan, T.Y. Wang, J. Guo, J.J. Richardson, F. Caruso, Synthesis of metal nanoparticles in metal-phenolic networks: catalytic and antimicrobial applications of coated textiles, Adv. Healthc. Mater. 7 (2018) 1700934.
[79] J. Xiong, X. Wu, Q. Xue, Biomolecule-assisted synthesis of highly stable dispersions of water-soluble copper nanoparticles, J. Colloid Interface Sci. 390 (2013) 41–46.
[80] M. Li, L. Gao, C. Schlaich, J. Zhang, I.S. Donskyi, G. Yu, W. Li, Z. Tu, J. Rolff, T. Schwerdtle, Construction of functional coatings with durable and broad-spectrum antibacterial potential based on mussel-inspired dendritic polyglycerol and in situ-formed copper nanoparticles, ACS Appl. Mater. Interfaces 9 (2017) 35411–35418.
[81] C. Chen, I. Ahmed, L. Fruk, Reactive oxygen species production by catechol stabilized copper nanoparticles, Nanoscale 5 (2013) 11610–11614.
[82] C. Yang, X. Ding, R.J. Ono, H. Lee, L.Y. Hsu, Y. Tong, J. Hedrick, Y. Yang, Brush-like polycarbonates containing dopamine, cations, and PEG providing a broad-spectrum, antibacterial, and antifouling surface via one-step coating, Adv. Mater. 26 (2014) 7346–7351.
[83] W. Zhang, S. Hu, J. Yin, W. He, W. Lu, M. Ma, N. Gu, Y. Zhang, Prussian blue nanoparticles as multienzyme mimetics and reactive oxygen species scavengers, J. Am. Chem. Soc. 138 (2016) 5860–5865.
[84] J.S. Ni, T. Min, Y. Li, M. Zha, P. Zhang, C.L. Ho, K. Li, Planar AIEgens with enhanced solid-state luminescence and ROS generation for multidrug-resistant bacteria treatment, Angew. Chem. Int. Ed. 59 (2020) 10179–10185.
[85] J. Hu, S. Liu, Modulating intracellular oxidative stress via engineered nanotherapeutics, J. Contr. Release 319 (2020) 333–343.
[86] J.R. Morones-Ramirez, J.A. Winkler, C.S. Spina, J.J. Collins, Silver enhances antibiotic activity against gram-negative bacteria, Sci. Transl. Med. 5 (2013), 190ra181–190ra181.
[87] L.Q. Chen, L. Fang, J. Ling, C.Z. Ding, B. Kang, C.Z. Huang, Nanotoxicity of silver nanoparticles to red blood cells: size dependent adsorption, uptake, and hemolytic activity, Chem. Res. Toxicol. 28 (2015) 501–509.
[88] C.Z. Liao, Y.C. Li, C.T. Sie, Bactericidal and cytotoxic properties of silver nanoparticles, Int. J. Mol. Sci. 20 (2019) 449.
[89] J. Guo, T. Suma, J.J. Richardson, H. Ejima, Modular assembly of biomaterials using polyphenols as building blocks, ACS Biomater. Sci. Eng. 5 (2019) 5578–5596.
[90] L. Yang, L. Li, H. Wu, B. Zhang, R. Luo, Y. Wang, Catechol-mediated and copper-incorporated multilayer coating: an endothelium-mimetic approach for blood-contacting devices, J. Contr. Release 321 (2020) 59–70.